ELSEVIER

Ceramics International 28 (2002) 527–540

CERAMICS INTERNATIONAL

www.elsevier.com/locate/ceramint

In-plane and interlaminar shear strength of a unidirectional Hi-Nicalon fiber-reinforced celsian matrix composite

Ö. Ünal[a], Narottam P. Bansal[b,*]

[a]*Ames Laboratory, Iowa State University, Ames, IA 50011, USA*
[b]*Materials Division, M.S. 106-5, NASA Glenn Research Center, Cleveland, OH 44135-3191, USA*

Received 9 November 2001; received in revised form 16 November 2001; accepted 26 November 2001

Abstract

In-plane and interlaminar shear strength of a unidirectional SiC fiber-reinforced $(BaSr)Al_2Si_2O_8$ celsian composite were measured by the double-notch shear test method between room temperature and 1200 °C. The interlaminar shear strength was lower than the in-plane shear strength at all temperatures. Stress analysis, using finite element modeling, indicated that shear stress concentration was not responsible for the observed difference in strength. Instead, the difference in layer architecture and thus, the favorable alignment of fiber-rich layers with the shear plane in the interlaminar specimens appears to be the reason for the lower strength of this composite. A rapid decrease in strength was observed with temperature due to softening of the glassy phase in the material. Published by Elsevier Science Ltd and Techna S.r.l.

Keywords: B. Composites; C. Mechanical properties; D. Silicate; E. Structural applications

1. Introduction

Barium strontium aluminosilicate $(BaSr)Al_2Si_2O_8$, commonly called celsian, is a potential matrix material for high temperature composites due to its low thermal expansion and excellent oxidation resistance [1]. Its most useful crystalline form is monoclinic since it is phase stable up to about 1600 °C [1–3]. Like many other ceramics, monolithic celsian is brittle and has relatively low flexural strength, ~130 MPa. However, fiber reinforcement with e.g. 42 vol.% of BN/SiC-coated continuous Hi-Nicalon SiC fibers not only drastically increases the flexural strength of the composite along the fiber direction, but also, failure occurs in a non-catastrophic manner [3].

Continuous fiber-reinforced composites are orthotropic materials with behavior that lies between those of isotropic and anisotropic materials [4]. Because the physical and mechanical properties are directional, the degree of this directionality strongly depends on the stacking sequence of fiber bundles. Therefore, the improvement to be realized in strength and failure behavior depends on how the composite is loaded with respect to principal material directions, in addition to the constituent properties and fiber/matrix interface bond strength. For example, since composites typically have low shear strength, shear failure could be dominant in the off-axis loading. Depending on composite architecture, such shear failures could take place either within the plane of composite, i.e in-plane, or within the plane of thickness, i.e. interlaminar [5]. These orientations are illustrated in Fig. 1. Therefore, to avoid unexpected failure and predict it beforehand by appropriate failure criteria, the factors affecting both shear strengths must be studied.

A number of test methods have been developed to study both in-plane and interlaminar shear properties. In-plane shear strength could be measured by an off-axis tension test [6], Iosipescu test [7–11], torsion test [12], etc. Interlaminar shear strength could be determined by short-beam test [13,14], Iosipescu test [10,11,15], double-notch method [16–20], etc. The shear test method should lead to a uniform shear stress distribution on the shear plane. For example, a torsion test, which provides a "true" pure shear stress state in thin walled-tubes, could not be used for plate

* Corresponding author. Tel.: +1-216-433-3855; fax: +1-216-433-5544.
E-mail address: narottam.p.bansal@grc.nasa.gov (N.P. Bansal).

0272-8842/02/$22.00 Published by Elsevier Science Ltd and Techna S.r.l.
PII: S0272-8842(02)00006-8

composites. Even if it were used, processing ceramic tube test specimens can be prohibitively expensive. The Iosipescu test, which leads to a "nearly" pure-shear state, and was standardized by the American Society for Testing and Materials (ASTM) for both polymeric [21] and ceramic composite materials [22], requires larger specimens. It is not suitable for elevated temperature testing with its present commercial metallic fixture.

In the material development stage it is common to use test methods which are simple and require small specimens, although they may not provide the desired uniform stress-state. The double-notched shear (DNS) test, where notches make the shear stress distribution in the specimen highly non-uniform [16–20], was used in this study. Since the DNS test is inexpensive, the ASTM standardized it for both plastic [23] and ceramic matrix composites [22]. The research community uses it frequently for comparative studies and quality checks. The DNS test was chosen in the present study because it allows the measurement of both in-plane and interlaminar shear strength by the same test specimen configuration. Moreover, the DNS test could be used at elevated temperatures.

Since the dimensions of the test specimens in this study were different from those in the ASTM Standard [22], and used by others [16–20], the first objective was to analyze the test specimen by finite element modeling (FEM). In light of the findings from stress analysis, the second objective was to carry out experiments up to 1200 °C to determine if there is a difference between in-plane and interlaminar shear strength of the celsian composite.

2. Stress analysis

Composite materials are anisotropic. The stress analysis requires constants which may not be readily available, particularly when the specimen material is new and made in small quantities. Fortunately, in such cases theoretical models could be used as alternative methods to estimate these constants from the constituent material properties. This approach, however, requires microstructural information including the number of constituents, constituent elastic constants, volume fractions, stacking sequence, and architecture of layers.

Fig. 1a and b, respectively, shows the interlaminar and in-plane shear specimens which are related by 90° rotation. The notches were made on the opposing faces perpendicular to the longitudinal axis, which is parallel to the fibers. The principal material directions were represented by the Cartesian coordinate system of 1, 2 and 3. As illustrated in Fig. 1, direction-1 is along the fibers while directions-2 and -3 are parallel to and perpendicular to the layers, respectively. Thus, extensional macroscopic engineering constants E_{11}, E_{22} and E_{33} represent the material coordinate system. Figs. 2a and b show optical micrographs of the composite perpendicular to and parallel to the fiber axis, respectively. It is clear that the composite microstructure contains distinct regions made up of periodic "fiber-rich" and "matrix" layers. Although such a layered microstructure is unusual in unidirectional composites, it should be taken into account during stress analysis and evaluation of experimental strength values.

2.1. Determination of macroscopic elastic constants

In the interlaminar specimen (Fig. 1a), the layers are perpendicular to the plane of the figure, i.e. parallel to imaginary shear plane between the notches. In the in-plane specimen (Fig. 2b), however, the layers are in the plane of the figure, i.e. perpendicular to the shear plane between the notches. The first step in the calculations was the determination of the elastic constants of the matrix and fiber-rich layers. The second step was to carry out further calculations based on findings from the first step and the number of layers present in the composite to obtain macroscopic elastic constants.

The polycrystalline celsian matrix layer is isotropic and its two elastic constants are already known, so no additional calculations were necessary for it. For the unidirectional fiber-rich layer (laminae), however, in-plane elastic constants E_L, E_T, υ_{LT}, and G_{LT} were needed (L and T stand for longitudinal and transverse,

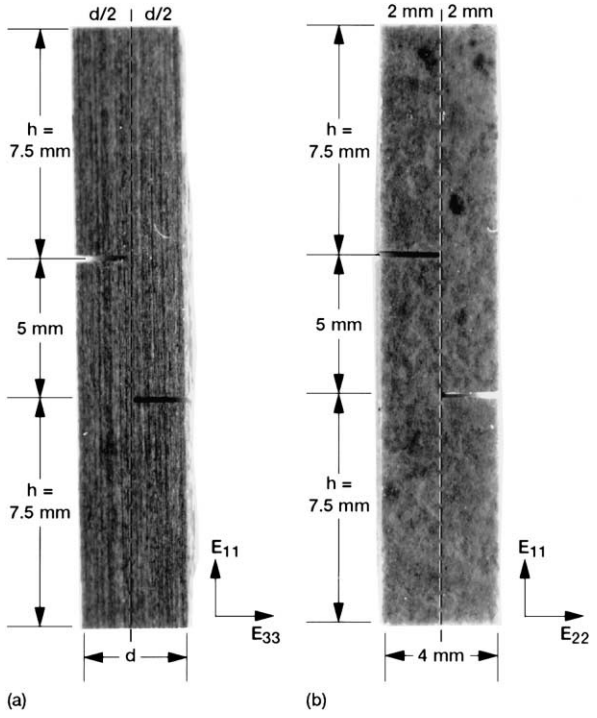

Fig. 1. Double notched shear (DNS) test specimens used in the current study: (a) interlaminar and (b) in-plane. Notice that they are related by 90°.

respectively). For this, the constituent properties in Table 1 were used. Since the fiber-rich layer had duplex coated fibers (nominal coatings thickness 0.4 μm BN and 0.1 μm SiC), in addition to the matrix, the elastic constant calculations were made in three steps; first, for the BN coating on the Hi-Nicalon fiber, then for the SiC coating on the BN coated fiber and finally, for the celsian matrix surrounding the duplex coated fiber. The calculations were made such that the values obtained in each step were used as input for the following step, while taking into account the volume fractions of the constituents involved. For example, in the final step of the calculation of the longitudinal elastic modulus for the fiber-rich layer, E_L, which was made for the celsian matrix, used the longitudinal modulus value obtained from the earlier step involving the SiC coating, $E_{L,f}$, and was carried out using the rule-of-mixtures in Eq. (1).

$$E_L = E_{L,f} V_f + E_m(1 - V_f) \quad (1)$$

where E_m is the elastic modulus of matrix and V_f is the fiber volume fraction in the fiber-rich layer, which was about 66%. Similarly, the calculation of the transverse elastic modulus for the fiber-rich layer, E_T, utilized the transverse fiber modulus obtained in the previous calculation step involving the SiC coating, $E_{T,f}$, and was done using the Halpin–Tsai equation[1] [4]:

$$E_T = E_m\left(\frac{1 + \xi\eta V_f}{1 - \eta V_f}\right) \quad (2)$$

where

$$\eta = \frac{(E_{T,f}/E_m) - 1}{(E_{T,f}E_m) + \xi}$$

ξ Is equal to 2 for circular fibers. Similarly, the in-plane shear modulus of the fiber-rich layer, G_{LT}, was calculated by Eq. (2) where E values were replaced by corresponding G values and ξ is equal to 1. The in-plane Poisson ratio, υ_{LT}, was calculated by the rule-of-mixtures similar to Eq. (1). The results of these calculations and volume fraction of the layers determined by the image analysis are shown in Table 2.

For the interlaminar specimen (Fig. 1a), the elastic constants needed for two-dimensional stress analysis were E_{11}, E_{33}, G_{13} and υ_{13}. Because of microstructural considerations in Fig. 2, elastic constants E_{11} and υ_{13} were calculated by Eq. (1) while E_{33} and G_{13} were obtained by Eq. (2) using data in Table 2. The results are shown in Table 3. It should be mentioned that the composite elastic modulus along the fibers, E_{11}, was also measured experimentally by strain gages and found to be 165 GPa. As can be seen in Table 3, the corresponding calculated value is 172 GPa, i.e. a discrepancy of $<5\%$. Considering the experimental uncertainties involving the measurements of volume fractions and elastic modulus values of the constituents, the agreement between the experimental and calculated values is very good.

For the in-plane specimen (Fig. 1b) the relevant elastic constants were E_{11}, E_{22}, G_{12} and υ_{12}. Since the layers are parallel to the plane of the figure it is best to use

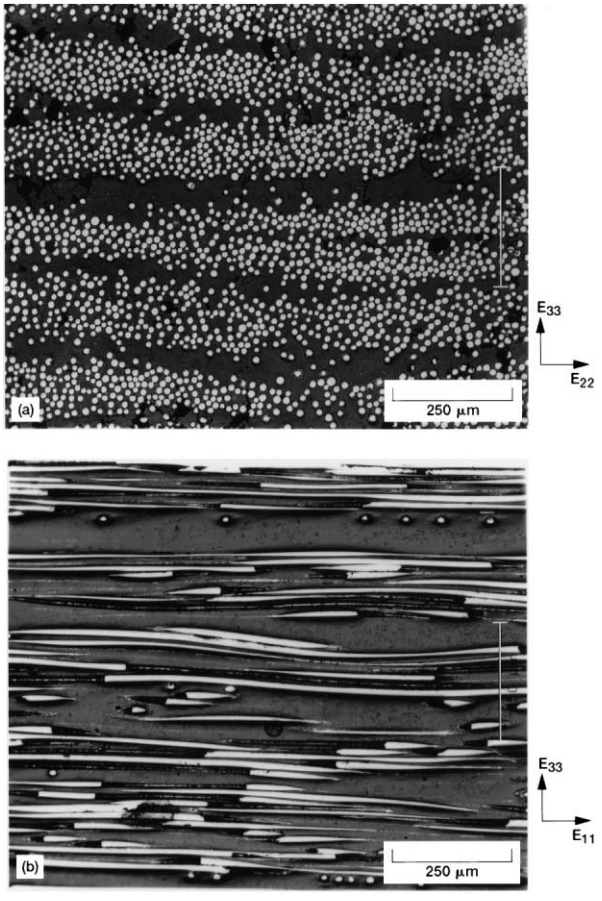

Fig. 2. Optical micrographs showing layered microstructure of the composites; (a) cross-sectional view, and (b) parallel to the fiber axis.

Table 1
Constituent elastic properties and volume fractions for the hi-nicalon fiber-reinforced celsian composite

Constituent	Elastic modulus (GPa)	Poisson's ratio	Volume fraction
Hi-Nicalon fiber	270	0.20	42%
Celsian matrix	96	0.32	51.8%
BN	62	0.17	4.9%
SiC	450	0.21	1.3%

[1] Halpin–Tsai equation is less accurate with fiber volume fraction approaching 1 [4], which was the case in calculations involving the coatings. However, since the calculations without coatings (only matrix and fibers) where fiber volume fraction was 0.42 also gave similar results, the degree of error may not be significant.

laminate theory to determine the macroscopic elastic constants. Laminate analysis requires stiffness of the matrix, the thickness and number of each layer, and the rotation angle between the principal material direction of each layer and the test specimen [4,24]. The components of stiffness of the matrix for both layers were already determined in Table 2. Since the fibers are along the test specimen axis, the rotation angle for the fiber-rich layer is 0°. For the matrix, the rotation angle is not an issue because of isotropy. The thickness of the fiber-rich and matrix layers was determined to be 90 ± 18 μm and 34 ± 13 μm, respectively. Using this information, the so-called extensional stiffness matrix A (3 ± 3) was determined. Macroscopic elastic constants for the in-plane (laminate) specimen were calculated by Eq. (3) [4].

$$E_{11} = \frac{A_{(1,1)}A_{(2,2)} - A_{(1,2)}^2}{A_{(2,2)}h} \tag{3a}$$

$$E_{22} = \frac{A_{(1,1)}A_{(2,2)} - A_{(1,2)}^2}{A_{(1,1)}h} \tag{3b}$$

$$v_{12} = \frac{A_{(1,2)}}{A_{(2,2)}} \tag{3c}$$

$$G_{12} = \frac{A_{(6,6)}}{h} \tag{3d}$$

where the indices in the parentheses show the location of components in the A matrix while h is the total specimen thickness. These results are also shown in Table 3. It should be mentioned that E_{11} calculated in Eq. (3a) agrees well with the value determined for the same constant by Eq. (1) in the interlaminar specimen.

Table 2
Calculated in-plane elastic constants for the layers in Fig. 2

Property	Fiber-rich layer	Matrix layer
E_L (GPa)	200	96
E_T (GPa)	174	96
υ_{LT}, υ_{TL}	0.24, 0.21	0.32
G_{LT} (GPa)	66	36
Volume fraction	0.73	0.27

The subscripts L and T indicate the longitudinal and transverse directions in the material coordinate system.

Table 3
Calculated elastic constants for the entire composite

Elastic constant	Value
E_{11}	172 GPa
E_{22}	153 GPa
E_{33}	149 GPa
G_{13}	56 GPa
G_{12}	58 GPa
υ_{13}	0.26
υ_{12}	0.25

Based on Figs. 1 and 2 and constituent properties in Table 1, one would expect the elastic modulus to be highest along the fiber direction (E_{11}) and lowest perpendicular to the layers (E_{33}), and intermediate parallel to the layers (E_{22}). In fact, the calculated values of E_{11} (172 GPa), E_{22} (153 GPa) and E_{33} (149 GPa) in Table 3 are in agreement with this prediction. Notice, however, that the ratios of E_{11}/E_{22}, and E_{11}/E_{33} in this composite are not as large as those in the polymer matrix composites. Moreover, the layered microstructure in Fig. 2 did not much affect the ratio of transverse modulus values ($E_{22}/E_{33}=1$ in the transversely isotropic composites). These results are believed to be due to the fact that the matrix elastic constants in the present composite are much larger and thus, a balance is present between the elastic constants and volume fractions of the Hi-Nicalon fiber, BN and SiC coatings, and celsian matrix. However, the above calculations showed that the modulus of the compliant BN coating, which was added to improve the fracture toughness by crack deflection, strongly affect the transverse elastic (E_{22} and E_{33}) and shear (G_{12}, and G_{13}) moduli. Therefore, the possible cracks in this coating as well as debonding at the fiber-matrix interface, which were not considered in these calculations, could significantly reduce these values, resulting in larger ratios of the longitudinal to transverse moduli.

2.2. Modeling

Linear-elastic FEM was carried out to determine the effect of specimen orientation on the stress-distribution between the notches. Two-dimensional plane-stress linear elastic analysis was carried out by a commercial package[2] using eight-node quadrilateral isoparametric elements with isotropic and orthotropic elastic properties. As boundary conditions, a uniform compressive load was applied along the specimen axis, and the specimen was allowed to deform laterally. The models utilized the real specimen dimensions. To capture actual notch geometry, the notches were modeled as semi-circles. Much finer mesh density was used at high stress regions surrounding the notches to improve the accuracy of calculations at these locations. Fig. 3a shows the overall finite element model while Fig. 3b and c illustrates comparison of the notch region in the actual specimen (interlaminar) and in the model, respectively. The elastic constants used in the interlaminar and in-plane specimen models were E_{11}, E_{33}, G_{13} and υ_{13}, and E_{11}, E_{22}, G_{12} and υ_{12}, respectively. Since specimen dimensions were the same, both models were loaded by the same uniform compressive stress along the fibers.

[2] ANSYS 5.5 University version, ANSYS Inc., Canonsburg, PA 15317, USA.

2.3. Comparisons of stress distributions

Fig. 4 shows the comparison of normalized shear stress distribution between the notches for interlaminar and in-plane specimens. The normalization was made by the average stress, τ_{ave}, between the notches, Eq. (4).

$$\tau_{ave} = \frac{P_a}{db} \tag{4}$$

where P_a is the applied force while b and d are the distance between notches and depth of the specimen, respectively. It is clear from Fig. 4 that the shear stress distributions in both specimens are not uniform. There is a high shear stress concentration near the notches, which is about 5.6 and 5.5 for the in-plane and interlaminar specimens, respectively. At exact notch roots, however, the shear stress is zero, because at these points the stress changes sign due to asymmetry in the notch geometry. Between the notches the shear stress decreases rapidly. Very similar shear stress distributions in the interlaminar and in-plane specimens imply that any difference between the experimental strength values between these specimens should not be attributed to the difference between shear stress distributions, but to other factors. This point will be discussed in detail later.

Fig. 5 shows the distribution of stress components between the notches in the interlaminar specimen.[3] The stress values were normalized by the applied uniform stress, σ_a. As can be seen, the stress concentration, σ_y, near the notch roots is close to five times the shear stress concentration, τ_{xy}. Stress concentration along the x-direction, σ_x, is similar to that of τ_{xy}.[4] Notice, however, that both σ_x and σ_y stress concentrations are compressive. Therefore, the macroscopic failure of these specimens is expected to occur in shear between the notches.

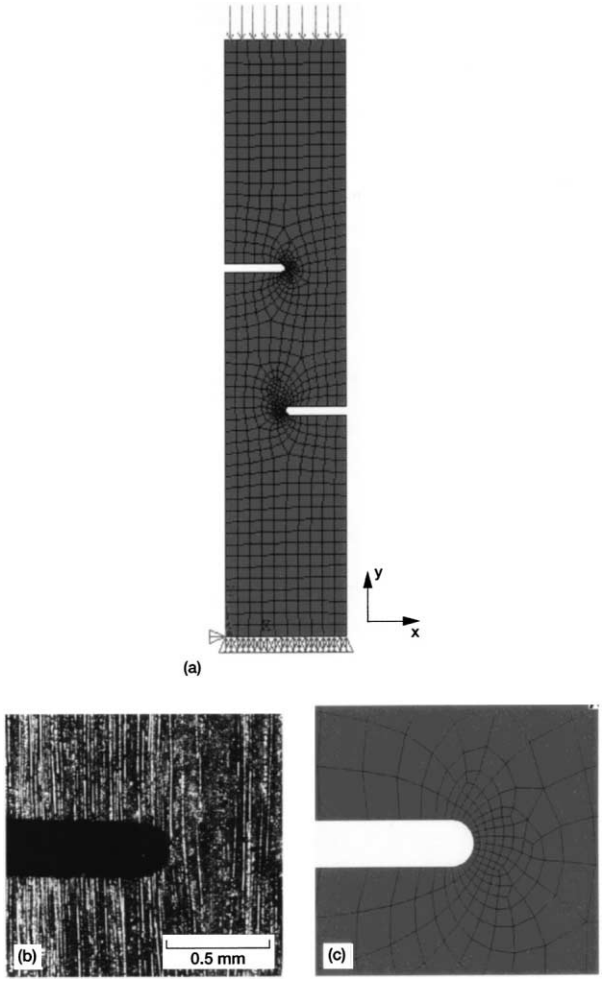

Fig. 3. Finite element model (a) of the DNS test specimen, and comparison of the notch geometry in the actual interlaminar specimen (b) and model (c).

3. Experimental procedure

Hi-Nicalon[5] fibers, with an average diameter of 14 μm, were used as reinforcement. Prior to processing, the fiber surfaces were coated with ~0.4 μm BN followed by ~0.1 μm SiC by chemical vapor deposition. The precursor to the celsian matrix of 0.75BaO–0.25SrO–Al_2O_3–$2SiO_2$ was made by solid-state reaction. The precursor powder consisted of mainly SiO_2 and $BaAl_2O_4$ with small amounts of Ba_2SiO_4, α-Al_2O_3 and $Ba_2Sr_2Al_2O_7$. This powder was made into a slurry with an organic solvent with various additives [25]. Tows of BN/SiC-coated fibers were impregnated with the matrix precursor by passing them through the slurry. The resulting prepreg tape was dried and cut into pieces. Unidirectional composites were prepared by tape lay up (20 plies) and warm pressing. Finally, dense composites were obtained by hot pressing under vacuum in a graphite die. X-ray diffraction showed that the precursor was fully converted into the desired monoclinic celsian phase through solid-state reaction. The fully dense composite was about 4 mm thick and had about 42 vol.% fiber.

Shear strength was measured using 4×4×20 mm DNS specimens (Fig. 1). The specimen cross-section was purposely made square to make one-to-one comparison between the in-plane and interlaminar shear strength values at a given test condition without the interference of possible specimen volume/shear area effect. Notches, which had 0.3 mm width, were extended exactly to the middle of the specimens, i.e. $d/2 = 2$ mm, to ensure that failure takes place on the plane between the notch tips. Notches were equidistant from the ends, and the distance between them was about 5 mm.

[3] Stress distribution was very similar in the in-plane specimen.

[4] Actual sign of shear stress between the notches is negative, as shown in Fig. 5. For convenience, shear stress values were shown as positive in Fig. 4.

[5] Nippon Carbon Co., Japan.

Dimensions of DNS specimens in this study were different from those recommended by the ASTM standard [22] because the test specimen in the standard has a rectangular cross-section and would not be suitable to study both in-plane and interlaminar shear strength. Moreover, a support fixture recommended in the standard to prevent possible buckling of specimens under compressive force was not utilized since lateral clamping of specimens could lead to artificially high shear strength values [17,22]. However, based on the recommendation of a previous study [16], the specimens were machined to have a height to thickness (h/d) ratio

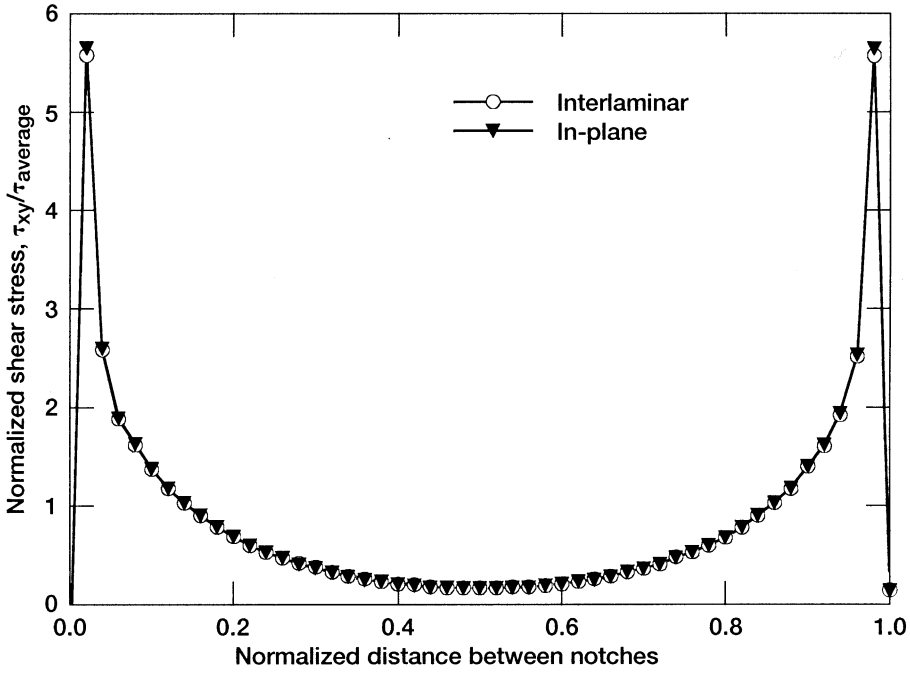

Fig. 4. Comparison of normalized shear stress distribution between the notches for interlaminar and in-plane specimens.

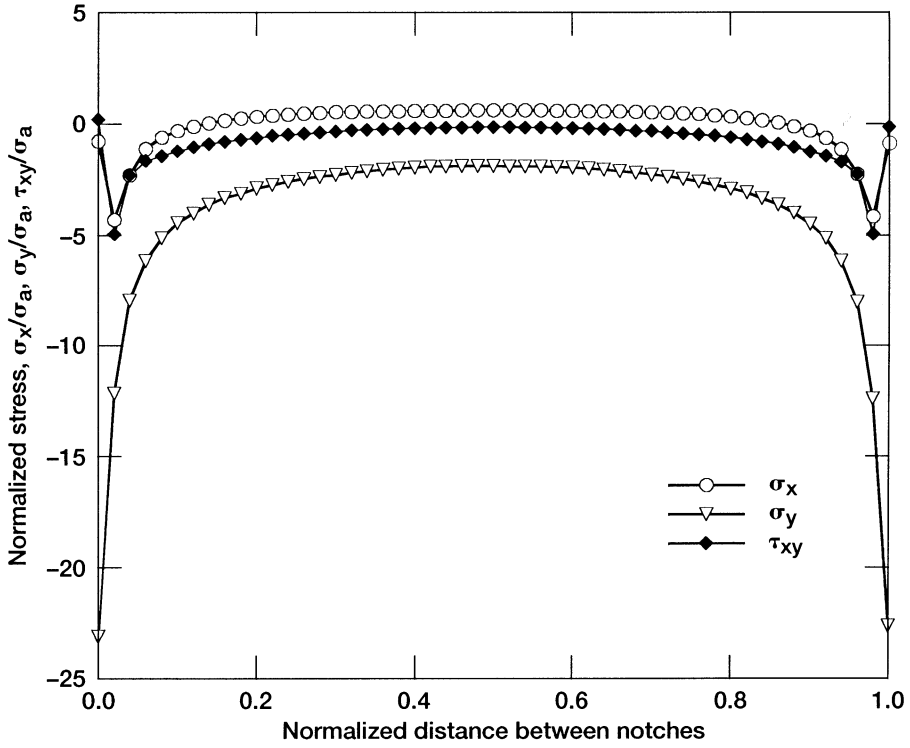

Fig. 5. Distribution of relevant stress components between notches in the interlaminar specimen.

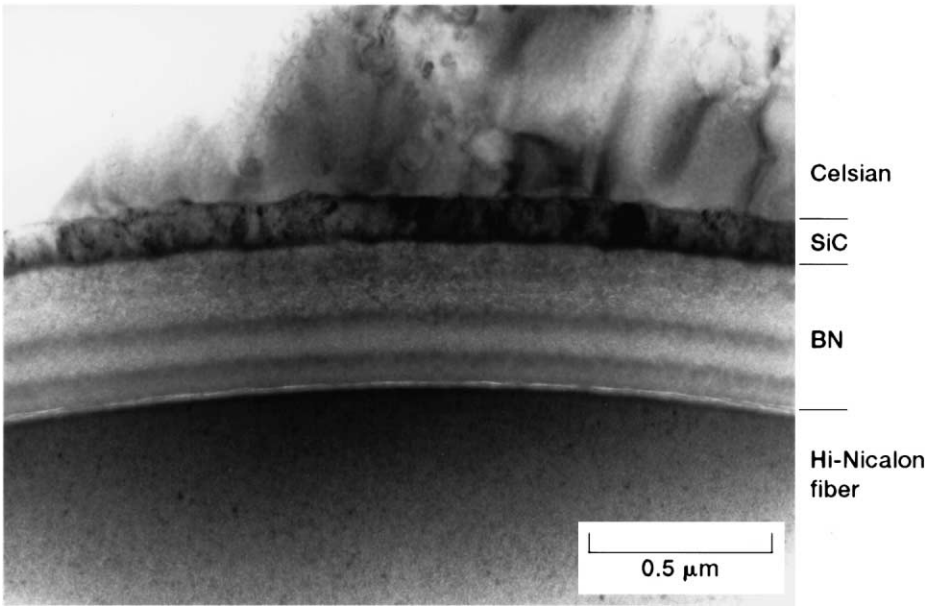

Fig. 6. TEM micrograph of interface region between Hi-Nicalon fiber and celsian matrix showing the duplex BN and SiC coatings. Notice that the BN coating consists of four layers.

of 1.87 to minimize buckling (Fig. 1). Buckling of specimens was checked by two strain gages which were mounted on the opposite lateral faces.[6] The difference in strain values from these two strain-gages was less than 3%, indicating that the buckling effect on strength values would be small. Force in both specimens was applied along the longitudinal axis by an MTS[7] machine in displacement control with a cross-head speed of 2 μm/s. Nine interlaminar and eleven in-plane shear specimens were tested up to 1200 °C in flowing N_2. Microstructural analysis was carried out by X-ray and transmission electron microscope (TEM). TEM specimens were prepared by conventional methods. An ion-beam thinner was used to obtain electron transparency in the specimens. Fractography was studied by scanning electron microscopy (SEM) and optical microscopy.

4. Results

4.1. Microstructure

Fig. 6 shows a typical TEM micrograph of a fiber with BN and SiC duplex coating and celsian matrix. The BN coating, which is amorphous, contains four successive layers and has an average total thickness of 0.4 μm. The SiC coating, however, is crystalline and has an average thickness of 0.1 μm. The BN layer was applied on the fiber surface to produce a compliant layer on the fiber and promote crack deflection away from the fibers while SiC was used to (i) form a diffusion barrier between BN and matrix, and (ii) to protect the fiber from damage during handling and composite processing [3]. The compilation of various data showed that the thickness of the coating along with the bond strength of the coating/matrix and coating/fiber interfaces play a critical role in determining the interlaminar shear strength of composites [26]. The X-ray diffraction (XRD) pattern taken from the polished section of composite, which is not shown here, showed monoclinic celsian as the only crystalline matrix phase, indicating that the thermodynamically stable monoclinic phase formed in situ from the mixed oxide precursor during hot pressing. The unstable and undesired hexacelsian phase was not present.

4.2. Mechanical properties

Fig. 7 shows the comparison of typical load versus displacement curves for the interlaminar and in-plane specimens at 1000 °C. There are three important points which need to be emphasized here. First, the in-plane shear strength was higher than the interlaminar shear strength. Second, the failure behavior was different: in the in-plane specimens the failure always took place in a catastrophic manner while in the interlaminar specimens it usually occurred in stages. Third, although the shear area between the notches was the same in both specimens due to their square cross-sections, shear stiffness of the in-plane specimens was usually higher than that of the interlaminar specimens. These observations were independent of the test temperature used, and buckling of specimens was not observed.

[6] Measurement Group, P-3500 unit was used.
[7] MTS System Co. Eden Prairie, MN, USA.

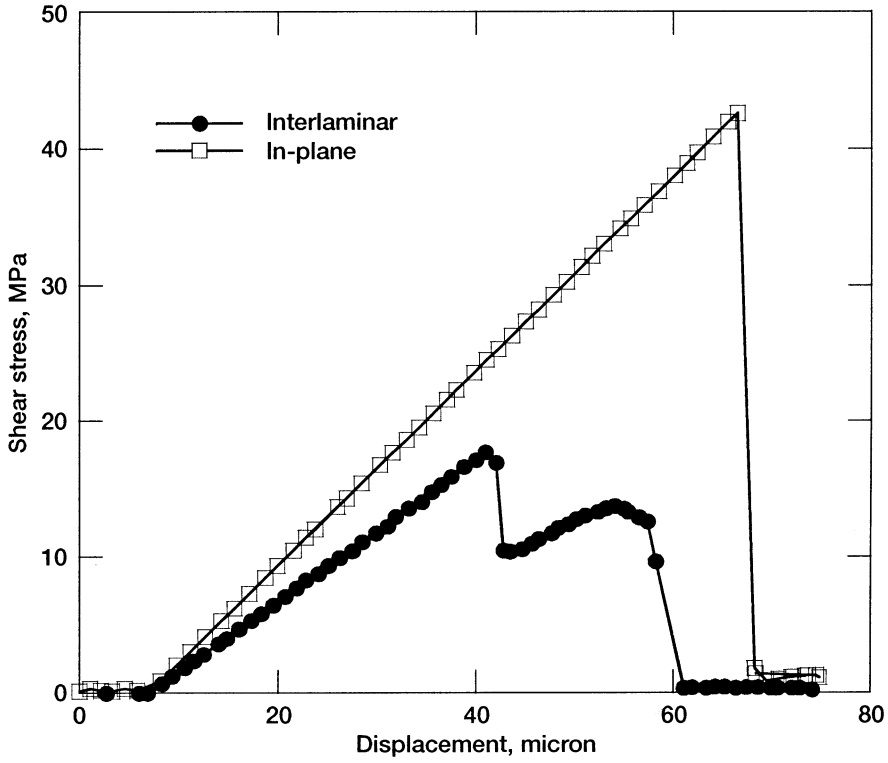

Fig. 7. Comparison of typical load versus displacement curves of the interlaminar and in-plane specimens at 1000 °C.

The results of the shear strength tests of both specimens as a function of temperature are shown in Fig. 8. The shear strength values reported here are the average stress between notches, τ_{ave}, which were calculated at maximum force by Eq. (4). Although Eq. (4) does not provide the intrinsic strength of the material, due to non-uniform stress distribution between the notches, it was useful here since the goal was to compare the strength values of these two specimens under identical testing conditions. It is clear from Fig. 8 that the in-plane shear strength is higher than the interlaminar shear strength regardless of temperature. Another important finding is that the shear strength decreased with temperature for both specimens, which appears to be pronounced above 600 °C.

Fractography showed some important differences. Fig. 9a and b are typical SEM micrographs of interlaminar and in-plane shear specimens, respectively, tested at 25 °C. The examination of notch regions in the interlaminar specimens showed that the failure always occurred within the fiber-rich region, a strong indication that the fiber-rich layer was weaker. Notice also in Fig. 9a that there is a region where the fibers bridge the shearing surfaces. This is because the fiber-rich layers were not always parallel to the specimen axis, or the shear plane between the notches, i.e. some misalignment was present. As a result, cracks from the notches could not link up on the same shear plane although the notch roots were exactly in the middle of the specimens. Since the fibers are stronger than the matrix, the bridging fibers prevented catastrophic failure and continued carrying some of the load beyond its peak value. In fact, this was the reason why the load/displacement curves in the interlaminar specimens exhibited steps (Fig. 7). Such failure features were also reported in the interlaminar specimens of carbon/epoxy composites [27]

Fracture features in the in-plane specimens were markedly different as the complete separation of the specimen across the shear plane always occurred. This is because the shear plane in these specimens is perpendicular to fiber-rich layers; thus, any misalignment between the fiber-rich regions and specimen axis was not critical. As a result, the failure took place catastrophically at maximum force (Fig. 7). Moreover, the in-plane specimens contained secondary cracks around the primary crack. Secondary cracks are believed to have occurred by the sudden release of elastic strain energy at peak force. Since no such cracks were observed in the interlaminar specimens, this indicates that the strain energy stored in the in-plane specimens during loading was higher. The comparison of stored elastic energy in Fig. 7, which is proportional to the area under the loading curve, is in agreement with this assessment. Fig. 10 shows an important failure mode in the interlaminar specimen and has a significant implication as to whether or not the stress concentration at the notches or the location of a critical flaw determines where the fracture takes place. The crack on the left originated at

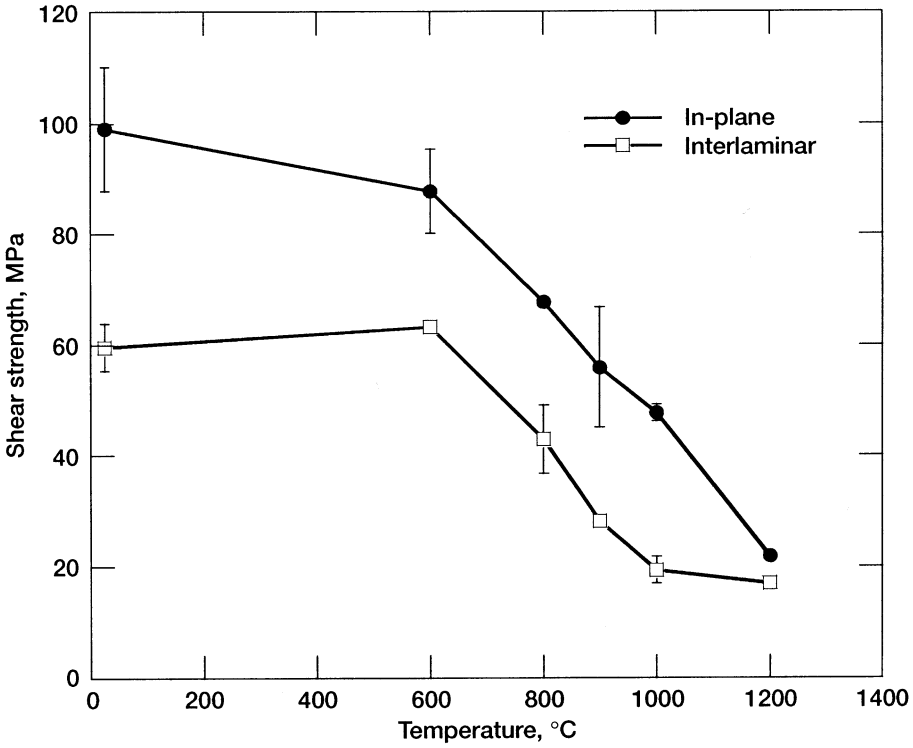

Fig. 8. Temperature dependence of the shear strength of interlaminar and in-plane specimens.

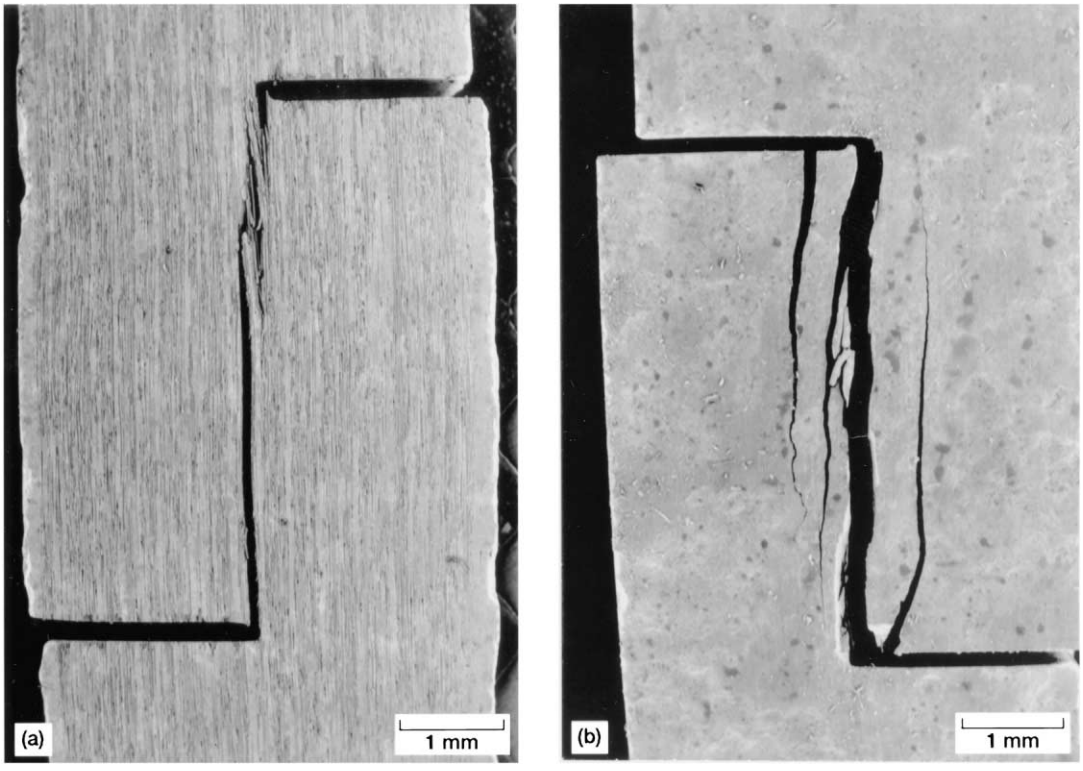

Fig. 9. SEM micrographs showing typical shear fracture features in the (a) interlaminar and (b) in-plane specimens tested at room temperature.

the tip of the notch at the bottom; however, the crack on the right did not start at the tip of the top notch but surprisingly away from it, perhaps at a weaker site associated with the fiber-rich region. Results from such specimens were not included in Fig. 8, although the values were not much different.

4.3. Effect of test temperature

To determine why the shear strength decreased with temperature (Fig. 8), the shear planes and microstructure were studied. The comparison of fracture planes in the interlaminar shear specimens, which were tested at 25 and 1200 °C, are shown in Fig. 11a and b, respectively. The failure in both specimens occurred in the fiber rich layers. Notice that the surface of the room temperature specimen (Fig. 11a) is relatively clean and cracks between the fibers and matrix fragments are clearly visible. The surface of the high temperature specimen (Fig. 11b), however, has a distinct phase which wetted the shear plane and glued the matrix fragments to the fibers.

Because shear strength also decreased in the in-plane specimens, their fracture surfaces were also studied. However, these observations were not conclusive because of the alternating layers, and thus, thin foils were prepared for TEM. A typical dark field TEM micrograph is shown in Fig. 12. As marked, the pockets of amorphous phase were found between the celsian grains. Similarly, such a phase was also observed near the fibers in the fiber-rich layers. Since the amorphous glassy phase typically softens at intermediate temperatures, failure takes place at a lower external force through sliding of matrix grains and fibers. Therefore, reduction in shear strength with temperature in Fig. 8 is believed to have occurred due to the softening of this amorphous phase. Such strength degradation by amorphous phase in ceramic systems is common and was observed previously by others as well [28]. The deformation of grains through dislocation plasticity is unexpected since the temperature range in this study was not high enough for the activation of dislocation motion. Depending on the differences between the thermal expansions of constituents, the residual stresses could also affect the strength below the processing temperature. However, the residual stresses could not be responsible for the observed reduction in strength with temperature here since their magnitudes are reduced with temperature. The difference in strength reduction with temperature in Fig. 8 may be related to the amorphous phase content on the corresponding fracture planes of these two specimens.

It should also be mentioned that although strength decreased substantially with temperature as a result of softening of the grain boundary phase, the load/displacement curves did not reveal substantial nonlinear deformation features. One possible reason could be that the strain rate used in this study is high for such an observation.

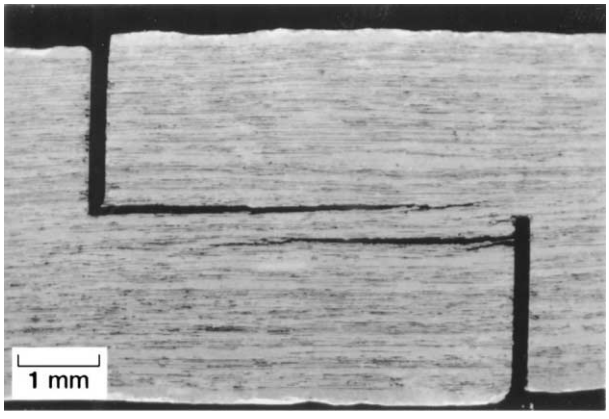

Fig. 10. SEM micrograph showing a failed interlaminar specimen. Initiation of an unusual shear fracture away from the notch indicates that the location of failure is determined by the local stress-state associated with the critical defect in the fiber-rich regions rather than the stress concentration near the notches.

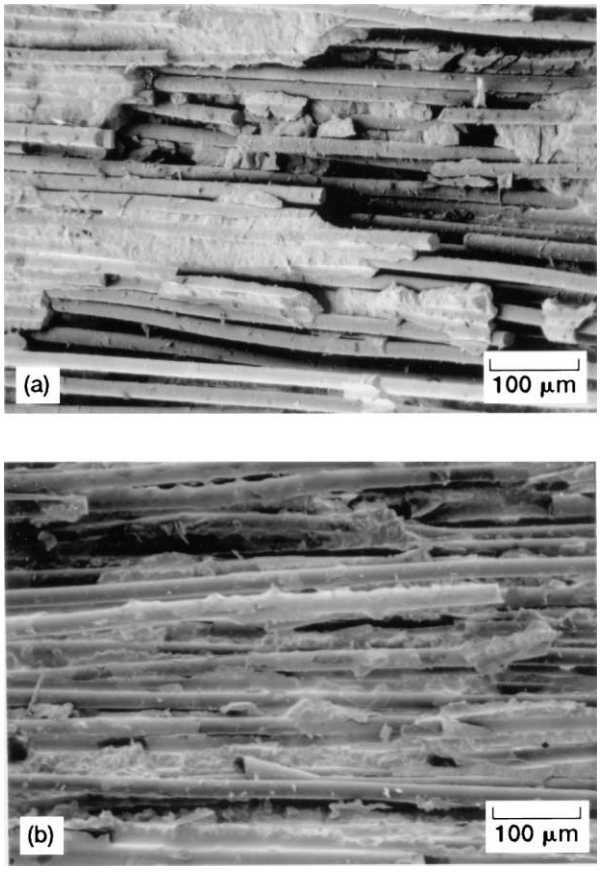

Fig. 11. SEM micrographs showing fracture surfaces of interlaminar specimens tested at (a) room temperature and (b) 1200 °C. Notice the absence and presence of a viscous phase in (a) and (b), respectively.

5. Discussion

5.1. Effect of anisotropy on stress distribution in DNS specimens

Distribution of stresses in DNS specimens have been shown to be dependent on such variables as the notch separation [16–20], notch depth [20], specimen width [16], notch distance from the specimen ends [16,17] and the presence/absence of support fixture [17,22]. Thus, it was recommended that experimental strength measurements involving non-standard DNS specimens should be complemented by stress analysis [17]. Stress analysis of current specimens showed that shear stress distributions are non-uniform and there are large stress concentrations at the notches (Fig. 4).

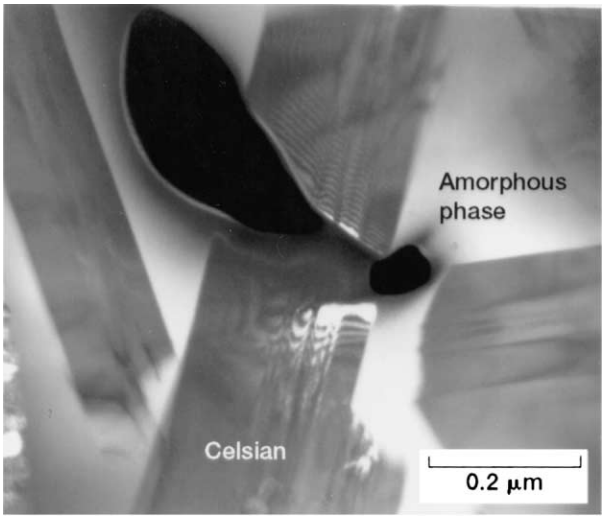

Fig. 12. Dark field TEM image showing the amorphous grain boundary phase between the grains of celsian matrix.

Another variable which affects stress distribution in the DNS specimen is anisotropy, although this was not very obvious in Fig. 4 due to a small difference between the elastic constants of in-plane and interlaminar specimens. To demonstrate the effect of anisotropy on the shear stress distribution and its possible implications, two transversely isotropic unidirectional composites were compared with an isotropic material. The degree of anisotropy in these composites is represented by E_{11}/E_{33} (or E_{11}/E_{22}) [16]. Graphite fiber reinforced ($E_{11}/E_{33}=12.8$) and glass fiber reinforced ($E_{11}/E_{33}=3.3$) polymer composites were chosen because their elastic constants are well characterized and anisotropy between them is large enough for discussion here [29]. Note that anisotropy in the current specimens was small in spite of its layered microstructure, i.e. $E_{11}/E_{22}=1.12$ for the in-plane and $E_{11}/E_{33}=1.15$ for the interlaminar specimens, and it was nearly transversely isotropic, i.e. $E_{22}/E_{33}=1$. For isotropic material, celsian was selected. The elastic constants used in the analysis were $E_{11}=155$ GPa, $E_{22}=E_{33}=12.1$ GPa, $G_{12}=G_{13}=4.4$ GPa and $\upsilon_{12}=\upsilon_{13}=0.248$ for the graphite composite, and $E_{11}=50$ GPa, $E_{22}=E_{33}=15.2$ GPa, $G_{12}=G_{13}=4.7$ GPa and $\upsilon_{12}=\upsilon_{13}=0.254$ for the glass composite. Elastic constants for celsian were $E=96$ GPa and $\upsilon=0.32$ (Table 3).

Fig. 13 compares the behavior of different types of materials. It is clear that anisotropy has a strong effect on the stress distribution, particularly on the stress

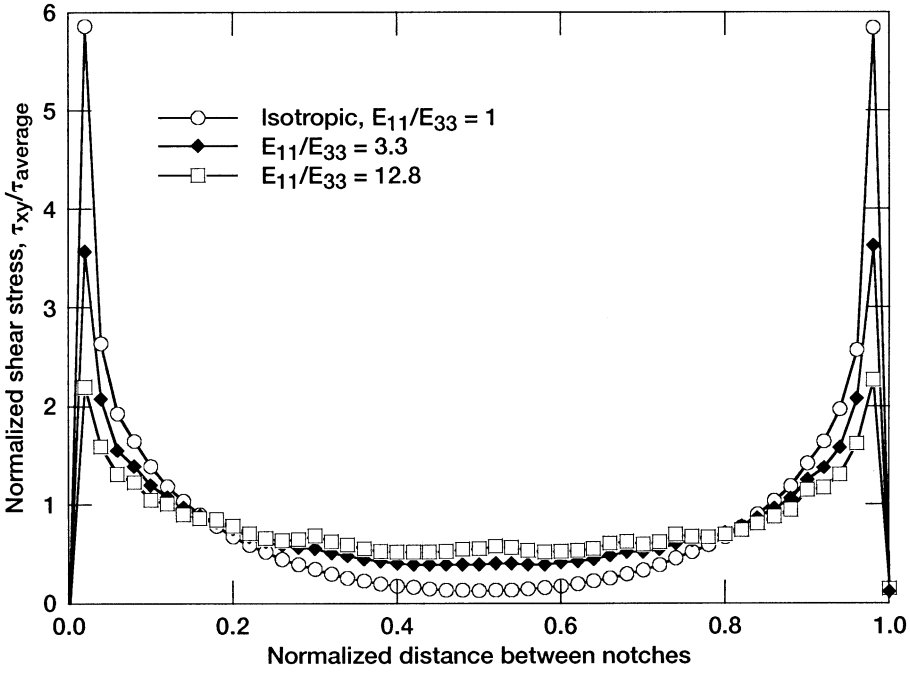

Fig. 13. Effect of material anisotropy on the shear stress distribution between the notches.

concentration near the notches. Stress concentration was largest in celsian (~5.8), intermediate in the less anisotropic glass composite (~3.6) and smallest in the most anisotropic graphite composite (~2.3). Such findings and trends are in agreement with a similar stress analysis involving the S-glass/epoxy, graphite/epoxy and graphite/polyimide composites [16], where the E_{11}/E_{33} ratios of the composites were 2.4, 7.3 and 43.2, respectively. Notice in Fig. 4 that shear stress concentration in the present composite was ~5.6, which is not much different from that of celsian in Fig. 13. This analysis clearly shows that anisotropy of the unidirectional composite reduces the stress concentration at the notches, and as a result, makes the stress distribution much more uniform. The decrease in stress concentration with anisotropy in Fig. 13 should not be surprising since the smaller lateral stiffness E_{33} (or E_{22}) material increases the lateral deformation. The implication of Fig. 13 is that the DNS specimen produces better quality strength data if the test involves the composite with large anisotropy, assuming that the specimen is loaded along the stiffest E_{11} direction. The strong effect of anisotropy on the stress distribution of composites was also shown in the Iosipescu specimen [10].

5.2. Interlaminar versus in-plane shear strength

Since the notch magnifies the effect of far-field applied force, the stress concentration associated with it could have a big impact on the measured strength values. In fact, such impact in DNS specimens was demonstrated in ceramic composites where the strength decreased with the magnitude of stress concentration as well [16,19].

In this study, the stress concentration in both specimens was almost the same in spite of the layered microstructure.

$$K_{t,\text{interlaminar}} \cong K_{t,\text{in-plane}} \tag{5}$$

Based on stress concentration alone, one would have expected the interlaminar and in-plane shear strength to be similar. However, results in Fig. 8 showed that the interlaminar strength was lower than in-plane strength at all temperatures, i.e.,

$$\tau_{13\ (\text{interlaminar})} < \tau_{12\ (\text{in-plane})} \tag{6}$$

This discrepancy between the prediction and the experiments indicates that the stress concentration could not be responsible for the difference observed in strength values. Moreover, even if the calculated elastic constants in Table 3 had underestimated the "actual" anisotropy[8], this conclusion would have still been valid since the anisotropy, which is higher in the interlaminar orientation, is expected to reduce the stress concentration and thus increase the strength of interlaminar specimens. Since this was not the case in the experiments, this clearly excludes the stress concentration as the possible reason for the difference in strength.

Instead, other factors such as microstructural features including the size and location of the strength limiting cracks and pores, which are not included in the continuum stress analysis, are believed to be responsible for the strength difference. In the 0/90° composites, for example, the difference between the in-plane and interlaminar shear strength was attributed to the presence/absence of interactions between the matrix crack with fibers [5]. In the interlaminar specimen this interaction is weak while in the in-plane specimens it is strong; as a result, the in-plane shear strength is always higher than the interlaminar shear strength in 0/90° composites [5]. The same types of interactions with fibers are not expected here because the present composite is unidirectional (no 90° fiber-bundles) and shear planes in both specimens are parallel to the fibers.

As indicated earlier, the failure in the interlaminar specimens always occurred within the fiber-rich layer which is the multiphase region with a high density of defects and grain boundaries. So, the process induced defects such as cracks and pores are often found at the fiber/matrix interface where initiation and growth of delamination cracks could take place when the crack path is parallel to applied stress, such as shear forces [17]. An important observation on the critical role of the defective fiber-rich region on the shear failure of an interlaminar specimen was already shown in Fig. 10. The fact that the crack initiated away from the notch in Fig. 10 clearly indicates that the location of the failure and the apparent strength of the composite is determined not by the high stress concentration near the notch, but by local stresses near the most critical defect in the microstructure. Because such defects are contained within the fiber-rich layer, strength is determined by the orientation of this layer with respect to the shear plane: when it is parallel and perpendicular, it leads to low (interlaminar) and high (in-plane) shear strength values, respectively.

High defect concentration in the fiber-rich layers may also be indicated indirectly by the slope of the load/displacement curves in Fig. 7 where the interlaminar specimen is less stiff. Since stiffness is defined as displacement per unit load, this suggests that the ligament surrounding the shear plane in the interlaminar specimens contains a higher fraction of the compliant part in the composite, i.e. fiber-rich layers. Although the difference is small, the calculated shear modulus values in Table 3 also show a similar tendency, i.e. 58 and 56

[8] Equations used to calculate unknown elastic constants assume perfect bonding at the interfaces and no porosity/cracks at the interface and in the matrix. Therefore, actual constants are expected to be different from those in Table 3 based on the deviation from the assumed case.

GPa for the in-plane and interlaminar specimens, respectively.

Fig. 5 showed that normal stress components σ_x and σ_y on the shear plane are compressive. However, in a real microstructure containing cracks and pores, both shear and tensile stress components could be present,[9] i.e. mixed mode. Assuming the presence of a small pre-crack within the fiber rich layer, the stress intensity values of interest are K_{II} and K_I, i.e. Mode-II and Mode-I, respectively. With the condition that the crack does not deviate from the original plane, which is expected here since the crack plane is parallel to the fibers, the fracture condition for mixed-mode loading is given by [30]:

$$\left(\frac{A\tau\sqrt{\pi a_c}}{K_{IIc}}\right)^2+\left(\frac{B\sigma\sqrt{\pi a_c}}{K_{Ic}}\right)^2=1 \quad (7)$$

where A and B are the geometric factors, a_c is the critical crack size and K_{IC} and K_{IIC} are the critical values of stress intensity. So, the failure is expected to initiate at a critical crack whenever the combination of shear stress τ and tensile stress σ satisfy the above condition. Note that regardless of mode-mixity, Eq. (6) shows that stress to failure (strength) is inversely proportional to crack length, which means that the material with the largest initial crack would likely have lower strength. Therefore, the difference between shear strength of in-plane and interlaminar specimens could be attributed to the difference in the defect density on the corresponding shear planes in these two specimens, i.e. lower interlaminar shear strength is due to favorable orientation of the defective fiber-rich region with the shear plane. The area/volume could also have a big impact on the measured strength values of brittle materials. However, this is not expected to be important in this study since shear areas in both specimens were the same.

6. Conclusions

1. Stress analysis showed that the shear stress distributions in interlaminar and in-plane specimens were non-uniform and a large stress concentration was present at the notches. However, stress distributions in both specimens were almost the same due to similarities in the corresponding elastic constants. It was also shown that anisotropy of the unidirectional composite is important in stress distribution and reduces the stress concentration at the notches. The reason for high stress concentration in current specimens was due to relatively high E_{22} and E_{33}.
2. Interlaminar shear strength was lower than in-plane shear strength at all temperatures. Moreover, the interlaminar specimens failed in stages while the in-plane specimens fractured catastrophically at maximum load. This could be attributed to the difference in the layer architecture.
3. Comparison of results from stress analysis and experiments suggests that the difference between the strength in the two orientations cannot be explained by the differences in stress concentration, but rather is due to the favorable alignment of highly defective fiber-rich layers with the shear plane in the interlaminar specimens. Since these layers were perpendicular to shear plane, the strength of in-plane specimens was higher.
4. The strength of both in-plane and interlaminar specimens decreased with temperature above 600 °C. Microstructure analyses suggest that this was due to softening of the amorphous glassy phase in the material.

[9] Any failure away from the plane between notches, such as the one in Fig. 10, have more tensile component.

Acknowledgements

Thanks are due to Dr. Subodh K. Mital for his constructive comments on the manuscript, Daniel J. Barnard for his help during mechanical testing and John Setlock for his technical assistance during composite processing.

References

[1] N.P. Bansal, Solid state synthesis and properties of monoclinic celsian, J. Mater. Sci. 33 (19) (1998) 4711–4715.
[2] N.P. Bansal, C.H. Drummond, Kinetics of hexacelsian-to-celsian phase transformation in $SrAl_2Si_2O_8$, J. Am. Ceram. Soc. 76 (5) (1993) 1321–1324.
[3] N.P. Bansal, J.I. Eldridge, Hi-Nicalon fiber-reinforced celsian matrix composites: influence of interface modification, J. Mater. Res. 13 (6) (1997) 1530–1537.
[4] B.D. Agarwal, L.J. Broutman, Analysis and Performance of Fiber Composites, 2nd Edition, John Wiley & Sons Inc, New York, 1990.
[5] Evans, A.G., Zok, F.W., Mackin, T.J., in: S.V. Nair, K. Jakus (Eds.), The structural performance of ceramic matrix composites in high temperature mechanical behavior of ceramic composites, Butterworth-Heineman, Boston, 1995, p. 3.
[6] C.C. Chamis, J.H. Sinclair, Ten-degree off-axis test for shear properties in fiber composites, Exp. Mech. 17 (1977) 339.
[7] N. Iosipescu, New accurate procedure for single shear testing of metals, J. Mater. Sci. 2 (1967) 537.
[8] D.E. Walrath, D.F. Adams, The Iosipescu shear test as applied to composite materials, Exp. Mech. 23 (1983) 105.
[9] P. Brondsted, F.E. Heredia, A.G. Evans, In-plane shear properties of 2-D ceramic composites, J. Am. Ceram. Soc. 77 (1994) 2569.

[10] W.R. Broughton, M. Kumosa, D. Hull, Analysis of the Iosipescu shear test as applied to unidirectional carbon-fiber reinforced composites, Compos. Sci. Technol. 38 (1990) 299.
[11] D.F. Adams, D.E. Walrath, In-plane and interlaminar Iosipescu shear properties of various graphite fabric/epoxy laminates, J. Comp. Tech. Res. 9 (1987) 88.
[12] G.A. Foley, M.E Roylance, W.W. Houghton, Use of Torsion Tubes to Measure In-Plane Shear Properties of Filament Wound Composites, ASTM STP 1003, p. 208, American Society for Testing and Materials, West Conshohocken, PA, 1989.
[13] K.T. Kedward, On the short beam test method, Fiber. Sci. Technol. 5 (1972) 85.
[14] Ö. Ünal, N.P. Bansal, Temperature dependency of strength of a unidirectional SiC fiber reinforced $(BaSr)Al_2Si_2O_8$ celsian composite, in: J.P. Singh, N.P. Bansal, (Eds.), Advances in Ceramic Matrix Composites, IV, Am. Ceram. Soc., Westerville, OH, Ceram. Trans. 96, (1999) 135–147.
[15] E. Lara-Curzio and M.K. Ferber, Shear Strength of Continuous Fiber Ceramic Composites, ASTM STP 1309, American Society for Testing and Materials, West Conshohocken, PA, 1997, p. 31.
[16] P. Dadras, J.S. McDowell, Analytical and experimental evaluation of double-notched shear specimens of orthotropic materials, Exp. Mech. 30 (1990) 184.
[17] N.J.J. Fang, T.W. Chou, Characterization of interlaminar shear strength of ceramic matrix composites, J. Am. Ceram. Soc. 76 (1993) 2539.
[18] M.F. Markham, D. Dawson, Interlaminar shear strength of fiber-reinforced composites, Composites 6 (1975) 173.
[19] F. Sugiyama, K. Ogawa, T. Nishida, Evaluation of the shear strength of advanced ceramic composite materials, Int. J. Mater. Product Technol. 14 (1999) 272.
[20] M.M. Shokrieh, L.B. Lessard, An assessment of double-notch shear test for interlaminar shear characterization of a unidirectional graphite/epoxy under static and fatigue loading, Appl. Compos. Mater. 5 (1998) 49.
[21] Shear Properties of Composite Materials by the V-Notched Beam Method, in: Annual Book of ASTM Standards, Practice No. ASTM D5379–93, American Society for Testing and Materials, West Conshohocken, PA, 1993.
[22] Shear strength of continuous fiber-reinforced advanced ceramics at ambient temperatures, in Annual Book of ASTM Standards, Practice No. C1292–95a, American Society for Testing and Materials, West Conshohocken, PA, 1995.
[23] In-plane shear strength of reinforced plastics, in: Annual Book of ASTM Standards, Practice No. D3846–85, American Society for Testing and Materials, West Conshohocken, PA, 1995.
[24] A.K. Kaw, Mechanics of Composite Materials, CRC Press, New York, 1997, p. 221.
[25] N.P. Bansal, Strong and tough Hi-Nicalon fiber-reinforced celsian matrix composites, J. Am. Ceram. Soc. 80 (9) (1997) 2407–2409.
[26] E. Lara-Curzio, Properties of CVD ceramic matrix composites, in: Comprehensive Composite Materials Encyclopedia, Vol. 4, Pergamon, London, 2000 (Chapter 18).
[27] R. Kamiya, T.-W. Chou, Strength and failure behavior of stitched carbon/epoxy composites, Metall. Trans. 31A (2000) 899.
[28] G. Ziegler, J. Heinrich, G. Wotting, Review: relationship between processing microstructure and properties of dense and reaction-bonded silicon nitride, J. Mater. Sci. 22 (1987) 3041.
[29] M.W. Hyer, Stress Analysis of Fiber-Reinforced Composite Materials, WCB/McGraw Hill Press, New York, 1998, p. 58.
[30] D. Broek, Elementary Engineering Fracture Mechanics, 4th Edition, Martinus Nijhoff Publ., Boston, 1986, p. 374.